



# Optimization of active surface area of flower like MoS<sub>2</sub> using V-doping towards enhanced hydrogen evolution reaction in acidic and basic medium



Saikat Bolar<sup>a,b</sup>, Subhasis Shit<sup>a,b</sup>, J. Sharath Kumar<sup>a,b</sup>, Naresh Chandra Murmu<sup>a,b</sup>,  
R. Sankar Ganesh<sup>c</sup>, Hiroshi Inokawa<sup>c</sup>, Tapas Kuila<sup>a,b,\*</sup>

<sup>a</sup> Surface Engineering & Tribology Division, Council of Scientific and Industrial Research-Central Mechanical Engineering Research Institute, Durgapur, 713209, India

<sup>b</sup> Academy of Scientific and Innovative Research (AcSIR), Ghaziabad, 201002, India

<sup>c</sup> Research Institute of Electronics, Shizuoka University, 3-5-1 Johoku, Naka-ku, Hamamatsu, 432-8011, Japan

## ARTICLE INFO

### Keywords:

MoS<sub>2</sub>  
Doping  
HER  
Mott-Schottky analysis

## ABSTRACT

Two dimensional layered transition metal dichalcogenides (TMDS) have immense potential as inexpensive electro-catalyst for hydrogen evolution reaction (HER). Modification of crystal and electronic structure is a promising strategy to enhance the catalytic performance of TMDS. Herein, a colloidal solvothermal method was used to prepare the vanadium (V) doped MoS<sub>2</sub> (VMSd). The structural, morphological and chemical analysis confirmed the formation of highly pure and uniform VMSd nanoflower. Tuning of V content in MoS<sub>2</sub> successively improved its catalytic activity towards hydrogen evolution reaction (HER). As, evident from the polarization curve, the VMSd required low overpotential of 194 and 206 mV to achieve benchmarking current density of 10 mA cm<sup>-2</sup> in acidic and basic medium, respectively. Mott-Schottky analysis suggested that the flat band potential of MoS<sub>2</sub> differed upon V-doping, resulting in alteration of charge transfer ability at the electrode-electrolyte interface. The Fermi level shifted towards the conduction band with optimized V-doping and the band structure got modified effectively.

## 1. Introduction

Modern civilization is driven by state-of-art technology, where one of the crucial components is energy. The current source of energy is primarily dependent on fossil fuels; its steady depletion propelled the researchers to find out the alternative source of energy to fulfil the current energy demand [1]. The burning of fossil fuel is detrimental to the environment and thus, encouraged the scientific community to develop certain technologies of renewable and everlasting sources which can meet the energy demand and also produce surplus for future use. In order to address these issues, different renewable sources like wind, hydroelectric, nuclear, solar, geothermal, hydrogen energy, etc are identified as the alternative sources [1]. Among these, hydrogen energy seemed most reliable due to its high energy density and environmental friendliness as H<sub>2</sub>O is the only by-product after direct burning of hydrogen or its consumption in fuel cell [1,2]. However, the main issue lies with hydrogen energy is that only 4% of total hydrogen energy produced globally through electrolysis technique which is considered as one of the safest and efficient method of hydrogen production [2]. Therefore, hydrogen generation through water electrolysis is

an emerging research topic. Platinum is considered as best electro-catalyst for hydrogen evolution reaction (HER) due to its low over-potential and swift kinetics [3,4]. It also provides suitable platform for the simultaneous adsorption-desorption of the active species resulting in the formation of gaseous hydrogen via electrolysis. However, the main difficulty of using Pt-based electro-catalyst is its very high cost, which pushes the researchers in the quest of finding alternative and efficient electro-catalyst for water splitting [5].

Transition metal dichalcogenides (TMDS) are found to be promising electro-catalyst materials for HER [6,7]. Among the available TMDS, molybdenum disulphide (MoS<sub>2</sub>); a two dimensional material exhibits promising results due to its high surface area, superior adsorption capability, electrical conductivity and remarkable thermal stability [8]. Volcano plot illustrates that hydrogen adsorption free energy of MoS<sub>2</sub> lies very close to that of Pt (~ 0 eV) [9]. The S sites are susceptible towards hydrogen due to its electronic environment in presence of Mo within the crystal lattice of MoS<sub>2</sub>. Theoretically calculated adsorption free energy values enlightened that the S edges are prominent in the hydrogen adsorption than the (0001) basal plane [10–12]. The skeleton structure of MoS<sub>2</sub> has been widely modified to accomplish a perfect

\* Corresponding author at: Surface Engineering & Tribology Division, Council of Scientific and Industrial Research-Central Mechanical Engineering Research Institute, Durgapur, 713209, India.

E-mail address: [tkuila@gmail.com](mailto:tkuila@gmail.com) (T. Kuila).

<https://doi.org/10.1016/j.apcatb.2019.04.028>

Received 20 December 2018; Received in revised form 5 April 2019; Accepted 11 April 2019

Available online 20 April 2019

0926-3373/© 2019 Elsevier B.V. All rights reserved.

catalytic activity of MoS<sub>2</sub> by increasing its charge transferability as well as accessible edge active surface area [13,14]. The surface of the MoS<sub>2</sub> has been tuned to attain better electro-catalytic activity. For improved hydrogen adsorption, the density of the active sites is increased by exposing active edge planes at the surfaces [15–18]. Kibsgaard *et al.* demonstrated electro-deposition technique to modify the MoS<sub>2</sub> mesoporous architecture with exposed active edge sites [12]. Kong *et al.* presented a synthetic procedure for developing a MoS<sub>2</sub> thin film with the vertically aligned layer to expose the edges sites [19]. Kim *et al.* reported MoS<sub>2</sub> nanosheets decorated with Au metal to enhance the charge transport between the sheets [20]. Ye *et al.* demonstrated that on doping with cobalt, the MoS<sub>2</sub>/Graphene changed its morphology and as a consequence the intrinsic electrocatalytic activity of active sites got enhanced [21]. So, doping makes a great impact to moderate the MoS<sub>2</sub> catalytic property. It has found that metals like Mn, Cr can modify the band structure as well as the semiconducting property of MoS<sub>2</sub> [22,23]. Therefore, the literature study shows that several works on MoS<sub>2</sub> were carried out to improve the catalytic activity by controlling the geometry and structure through transition metal doping, which in turn improves the HER activity. Controlled transition metal doping improved the electronic mobility, charge transportability, catalytically active surface area and turnover frequency to facilitate the HER activity by lowering the overpotential value [24–33]. However, there is huge scope for modification of MoS<sub>2</sub> in order to achieve the HER catalyzing activity through doping. Transition metal like vanadium (V) can effectively enhance the HER activity of MoS<sub>2</sub> on doping. Moreover, the improved charge transfer ability effectively lowers the overpotential value. Furthermore, Fermi level shifted close to the conduction band level after V doping in MoS<sub>2</sub> [34]. The incorporation of V in the MoS<sub>2</sub> structure enhanced the free carrier density at the Fermi level, resulting in an elevation of catalytic property [35]. However, V-doping effectively enhances the electronic and optical property of MoS<sub>2</sub> through the modification of density of state (DOS) [36]. This type of modification affects the metallic behaviour of MoS<sub>2</sub> which subsequently improved the HER activity. Furthermore, the V-doping on MoS<sub>2</sub> enhanced the overall conductivities of the prepared materials.

Herein, a facile in-situ solvothermal method is demonstrated to synthesize V doped MoS<sub>2</sub> (VMSd) nanoflowers. Synthesized VMSd has been used as an electro-catalyst towards HER in both acidic and basic mediums. Overpotential of 194 and 206 mV were derived for VMSd composition at 10 mA cm<sup>-2</sup> in acidic and basic medium respectively. The presence of V in MoS<sub>2</sub> crystal lattice improves the charge transport between the sheets and enhances the HER catalytic efficiency effectively. So, the catalytic performance of MoS<sub>2</sub> is surprisingly improved by V-doping.

## 2. Experimental

### 2.1. Material

Sodium molybdate [Na<sub>2</sub>MoO<sub>4</sub>·2H<sub>2</sub>O], thiourea [CS(NH<sub>2</sub>)<sub>2</sub>], potassium hydroxide [KOH] and sulphuric acid [H<sub>2</sub>SO<sub>4</sub>] were purchased from Merck specialties Pvt. Ltd. Mumbai, India. Vanadyl acetylacetonate [VO(acac)<sub>3</sub>] and 10 wt % platinum on carbon [Pt/C] were purchased from Sigma Aldrich. Absolute ethanol was obtained from Honyon International Inc., China. All the mentioned chemicals were of analytical grade and used without further purification.

### 2.2. Synthesis of V doped MoS<sub>2</sub>

V doped MoS<sub>2</sub> (VMSd) was synthesized by a facile in-situ solvothermal method (as shown in the Scheme 1) using stoichiometric amount of precursors. Weighed amount of Mo and V salts were dissolved in 45 mL of mixed solvent containing water and ethanol in 2:1 ratio. Sulphur source was dissolved in 20 mL of distilled water separately and mixed dropwise to the metal salt solution under constant

agitation. Then, the solution mixture poured into a 100 mL Teflon-lined stainless-steel autoclave reactor. The autoclave reactor was locked properly and kept for 18 h inside a hot-air oven at 180 °C. Then it was allowed to cool normally to room temperature and the obtained product was collected after washing and filtration. The obtained materials were dried overnight inside a vacuum oven at -60 °C. Three different composition of VMSd were obtained by varying the ratio of V to Mo precursors as tabulated in the Table 1. For comparison, pure MoS<sub>2</sub> was also prepared by similar procedure without the addition of V salt.

### 2.3. Electrode fabrication

Measured amount of prepared materials were dispersed in 1:1 ethanol-water solution containing 10 wt % polyvinylidene fluoride (PVDF) and 10 wt % carbon black. The mixture was sonicated to obtain homogenous catalytic ink and then drop casted onto the clean and shiny glassy carbon electrode with a loading amount of 0.5 mg/cm<sup>2</sup>. For comparison, the state-of-the-art electrocatalyst Pt/C (10 wt % Pt content) was also drop casted onto the glassy carbon electrode.

### 2.4. Physicochemical characterization

Field emission scanning electron microscopy (FE-SEM) and energy dispersive X-ray spectroscopic (EDS) elemental mapping micrographs were obtained from Eigma HD, Carl Zeiss, Germany. X-Ray diffraction (XRD) patterns were recorded by D2 PHASER, Bruker, Germany, using Cu Kα radiation (λ = 0.15418 nm). X-ray photoelectron spectroscopy (XPS) was carried out using Shimadzu ESCA 3400. Transmission electron microscopy (TEM) was performed using JEM-2000RXII at 15 and 200 kV. UV–vis absorption spectra of dispersed nanoparticle solutions were recorded by a UV–vis spectrophotometer (1601SHIMADZU). Inductively coupled Plasma Atomic Emission Spectroscopy (ICP-AES) analysis was carried out with ARCOS, Simultaneous ICP Spectrometer.

### 2.5. Electrochemical characterization

All the electrochemical characterization were carried out using PARSTAT 4000 (Princeton Applied Research, USA). The electrochemical test were performed in both 0.5 M H<sub>2</sub>SO<sub>4</sub> and 1 M KOH solution. Three-electrode system was used for the electrochemical characterization with Ag/AgCl/saturated KCl, platinum wire and catalyst-loaded onto the glassy carbon as reference, counter and working electrode, respectively. The recorded potentials were later transformed into reversible hydrogen electrode (RHE) scale according to the following equation:

$$E_{\text{RHE}} = E_{\text{Ag/AgCl/Sat.KCl}} + 0.059 \text{ pH} + 0.197 \quad (1)$$

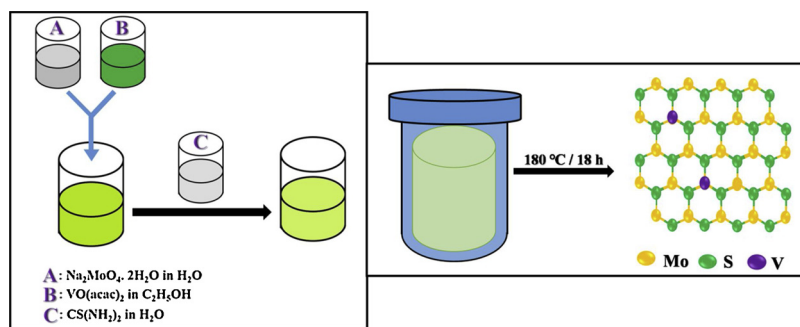
Several voltammetric cycles were performed at a scan rate of 100 mVs<sup>-1</sup> before recording the polarization curves. All the current densities obtained were normalized by dividing the obtained current response with the geometric area of the working electrode. Linear sweep voltammetry (LSV) was recorded at a low scan rate of 5 mVs<sup>-1</sup> to minimize the electrical double layer charging current [37,38]. The influence of uncompensated resistance was eliminated by iR correction. Tafel slope values were obtained from Tafel plot, which were derived from LSV curves. The Tafel slope analysis were performed using the following equation.

$$\eta = a + b \log j \quad (2)$$

Where,  $\eta$ ,  $j$  and  $b$  are overpotential, current density and Tafel slope, respectively. For HER overpotential ( $\eta$ ) = 0 -  $E_{\text{RHE}}$ .

Electrochemically active surface area (ECSA) and roughness factor (RF) were calculated from electrochemical double layer capacitance ( $C_{\text{dl}}$ ) value using the following equations:

$$ECSA = \frac{C_{\text{dl}}}{C_s} \quad (3)$$



Scheme 1. Schematic of VMSd preparation.

Table 1

Amount of precursors used for the preparation of various VMSd.

Amounts of Precursor (m mol)			Sample Name
Mo	S	V	
1	2.5	0.05	VMS1
1	2.5	0.1	VMS2
1	2.5	0.25	VMS3

$$RF = \frac{ECSA}{\text{Geometric Area of Electrode}} \quad (4)$$

$C_s$  is the specific capacitance of atomically smooth planar surface in respective electrolytic medium [39].  $C_s$  was considered to be  $40 \mu\text{Fcm}^{-2}$  and  $35 \mu\text{Fcm}^{-2}$  for 1 M KOH and 0.5 M  $\text{H}_2\text{SO}_4$ , respectively [40].  $C_{dl}$  values of all the material were calculated from multiple cyclic voltammetry (CV) scan with different scan rates ( $\nu$ ) within a very specific narrow potential window. The corresponding specific capacitance values were obtained by plotting  $\Delta j$  vs.  $\nu$  plot. Where,

$$\Delta j = (j_a - j_b)/2 \quad (5)$$

In order to check the stability of the electro-catalyst, about 1000 CV scan was performed with a  $100 \text{ mVs}^{-1}$  scan rate within a potential window of 0.00 to  $-0.35 \text{ V}$ . Chronoamperometric studies were performed by applying a constant potential to check the stability. Electrochemical impedance spectroscopy (EIS) was performed within frequency ranging from  $10^5$  to 0.1 Hz applying a sinusoidal alternating current (AC) along with DC potential bias of 10 mV to comprehend the dynamics of the electrochemical changes happening at the electrode-electrolyte interface. Nyquist plots obtained from EIS were fitted with Randles equivalent circuit using Z view® software (Scribner Associates Inc. USA). Mott-Schottky analysis was also performed to understand electrode electrolyte interfacial property. The flat band potential and doping density were calculated from Mott-Schottky plot.

### 3. Results and discussion

#### 3.1. FE-SEM image analysis

FE-SEM images were analyzed to understand the crystal growth mechanism and the morphology of the synthesised materials. Fig. 1 corresponds to the surface morphologies of the synthesised materials i.e. VMS2 and  $\text{MoS}_2$ . High resolution FE-SEM images of VMS2 and  $\text{MoS}_2$  showed the flower like architecture consisting of colossal petals with a common centre of adhesion. This kind of molecular arrangement has exposed active site, which helps to improve the hydrogen adsorption capability. The diameter of  $\text{MoS}_2$  nanoflowers having ultrathin petals was calculated to be  $\sim 2 \mu\text{m}$  (see in Fig. 1a). In-depth study showed that the petals of the nanoflowers had rough surface. It was also found that the  $\text{MoS}_2$  nanostructure retained its hierarchical nature even after V-doping. The morphology of pure  $\text{MoS}_2$  remained unaltered even after V-

doping in its crystal structure. The corresponding elemental mapping for VMS2 was also performed (as represented in the Fig. S1). It clearly indicated the presence of Mo, S and V in the prepared nanomaterials. It was also observed that the presence of V was minimalistic compared to Mo and S, which confirmed that the V played the role of dopant in the synthesised materials. Further the mapping analysis suggested that the doped V homogeneously distributed throughout the  $\text{MoS}_2$  crystal structure [41].

#### 3.2. TEM image analysis

In order to gain further information about the morphology of the prepared materials, TEM images were recorded and investigated. The petals of the nanoflowers were clearly visible in the TEM images of both  $\text{MoS}_2$  and VMS2 (as shown in Fig. 2a, b). HR-TEM image (as depicted in Fig. 2c) confirmed the layered lamellar structure of VMS2. Fig. 2d, e) demonstrates the Inverse Fast Fourier Transformation (IFFT) pattern at the R1 and R2 regions. The nanopetals of VMS2 were formed by ultra-thin  $\text{MoS}_2$  sheets. The interlayer spacing in between the  $\text{MoS}_2$  sheets was found to be 0.62 nm corresponds to (002) crystal plane. This observation is in good agreement with the previous study where spray drying method was employed to prepare  $\text{MoS}_2$  [41].

The lattice spacing value of 0.27 nm was calculated from the R2 region corresponding to the (100) crystal plane and this observation matched well with the reported data [42]. Fig. 2f represents the IFFT pattern recorded from the R3 region and revealed the presence of defects in  $\text{MoS}_2$  crystal structure. Interestingly, the lattice spacing of (002) and (100) crystal planes of VMS2 were comparable to that of  $\text{MoS}_2$ . It may be due to comparable ionic radius and electronic environment of V and Mo. Characteristic chevron like Mo-S-Mo bonding in VMS2 was observed in IFFT pattern at the R4 region as shown in Fig. 2g. Inspection of the HR-TEM images further confirmed the absence of  $\text{VS}_2$  lattice in VMS2. The absence of  $\text{VS}_2$  phase and any other composites with  $\text{MoS}_2$  concluded the exclusive doping of V ion in  $\text{MoS}_2$  crystal lattice. Although there may be the formation of infinitesimal amount of  $\text{VS}_2$  in VMSd but due to very small amount it was not detected through characterization techniques. Therefore, the basic skeleton structure of VMS2 composed of  $\text{MoS}_2$  nanoflower and the basic structure of VMS2 remained unaffected after V-doping as observed from the TEM image analysis.

#### 3.3. XRD analysis

XRD patterns (as shown in Fig. 3a) were analysed to investigate the crystal structure of all the synthesised materials. It showed a number of peaks at  $2\theta$  values of  $13.4^\circ$ ,  $32.2^\circ$ ,  $34^\circ$ ,  $43.1^\circ$  and  $53^\circ$  which can be ascribed to the (002), (100), (101), (006) and (110) crystal planes of pure  $\text{MoS}_2$ , respectively. The corresponding crystal planes suggested that the  $\text{MoS}_2$  is in hexagonal phase belonging to the  $P6_3/mmc$  space group as indexed in JCPDS card no: 37-1492 [33,41]. Bragg's Equation helped to calculate atomic plane spacing of the synthesized VMS2 nanoparticle.



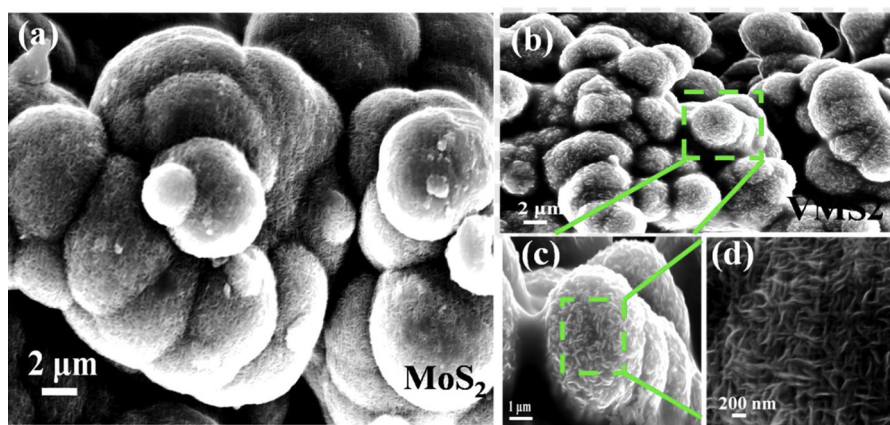


Fig. 1. a) FE-SEM image of MoS<sub>2</sub>; b), c) & d) FE-SEM micrograph of VMS2 at different magnifications.

$$2d\sin\theta = n\lambda$$

(6)

where,  $d$  is the atomic plane spacing,  $n$  is the order of diffraction,  $\theta$  is Bragg scattering angle and  $\lambda$  is the wave length of incident radiation. Interlayer spacing of (002) and (100) crystal planes of VMS2 matched well with the lattice spacing value obtained from the HR-TEM image analysis. The peaks corresponding to the (002) crystal plane shifted towards the lower  $2\theta$  value and the (100) plane to the larger value with the increment of doping concentration. It may be due to the expansion along (001) direction along with in-plane compression of the MoS<sub>2</sub> lattice. Uniaxial tensile strain was created along (001) direction after V-doping [43]. V atoms were incorporated in MoS<sub>2</sub> crystal structure as V<sup>2+</sup> ions have slightly higher ionic radius compared to Mo<sup>4+</sup> ions [44]. The (002) crystal plane shifted towards the lower angle, indicating gradual increase in (002) plane spacing [45]. No other characteristic peak was observed representing that the V atom was successfully doped in the lattice structure of MoS<sub>2</sub>.

### 3.4. XPS analysis

X-ray photoelectron spectroscopy (XPS) was performed to further

analyse the surface chemical composition, outer electronic configuration and exact oxidation state of the element. The survey spectra showed the presence of Mo, S, and V element in VMS2 (depicted in Fig. S2). From XPS survey analysis, the atomic percentage of V was found to be 1.66, 2.84 and 4.24 for VMS1, VMS2 and VMS3, respectively. The stoichiometric composition of VMSd were calculated and summarized in Table 2. A prominent peak at 285 eV observed in the survey spectra (Fig. S2) indicated the presence of adventitious carbon species arising due to surface adsorbed CO<sub>2</sub> and CO [46]. The chemical states of all elements (Mo, V and S) were recognized from the high resolution XPS profile. The deconvoluted peaks for Mo were found at 228.47 and 231.60 eV was ascribed to the Mo<sup>4+</sup> 3d<sup>5/2</sup> and Mo<sup>4+</sup> 3d<sup>3/2</sup>, respectively confirming the existence of Mo in MoS<sub>2</sub> as depicted in Fig. 3b. Two low intense peaks at -232.8 and 235.17 eV were noticed for Mo<sup>6+</sup> 3d<sup>5/2</sup> and Mo<sup>6+</sup> 3d<sup>3/2</sup> due to MoO<sub>3</sub> formation under air atmosphere [47]. No characteristic peak was recorded for Mo(0) state from XPS [48]. A small peak at -225.7 eV was found corresponding to the Mo-S bond [49]. In the high resolution XPS profile of S 2p (as shown in Fig. 3c), peaks corresponding to S 2p<sup>1/2</sup> and S 2p<sup>3/2</sup> at -161.63 and -163.2 eV, respectively, indicated the presence of S as S<sup>2-</sup> state [48]. A broad oxidized sulphur peak detected at -168.3 eV due to the oxidation

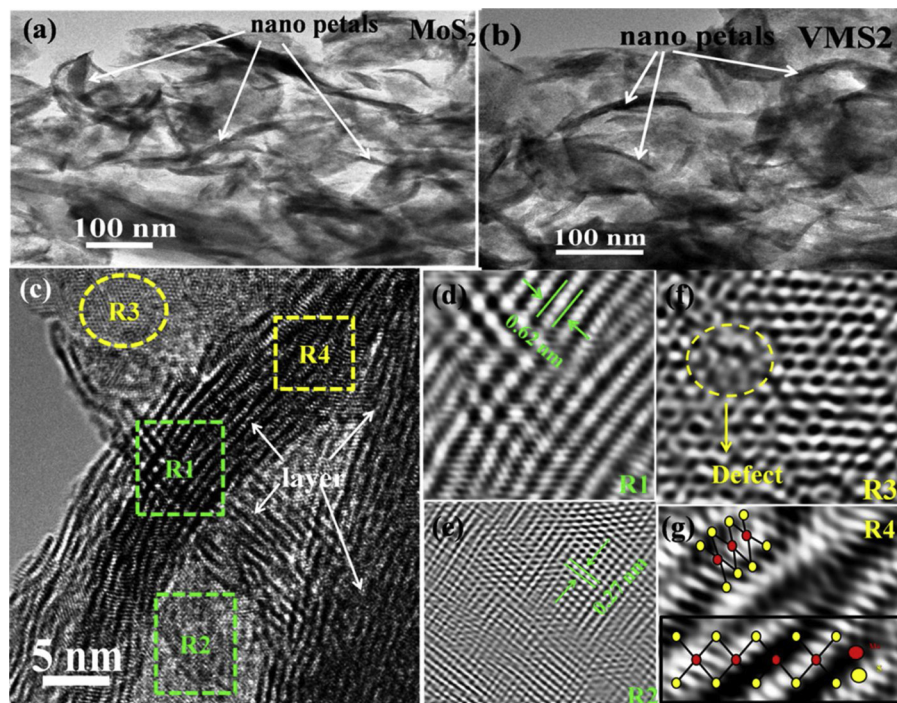


Fig. 2. a, b) TEM images of MoS<sub>2</sub> & VMS2; c) HR-TEM micrograph showing a few layer VMS2 and IFFT images of the d) R1, e) R2, f) R3 (with yellow circle indicating the area of defects) & g) R4 (showing Mo-S-Mo bonding) regions (For interpretation of the references to colour in this figure legend, the reader is referred to the web version of this article).

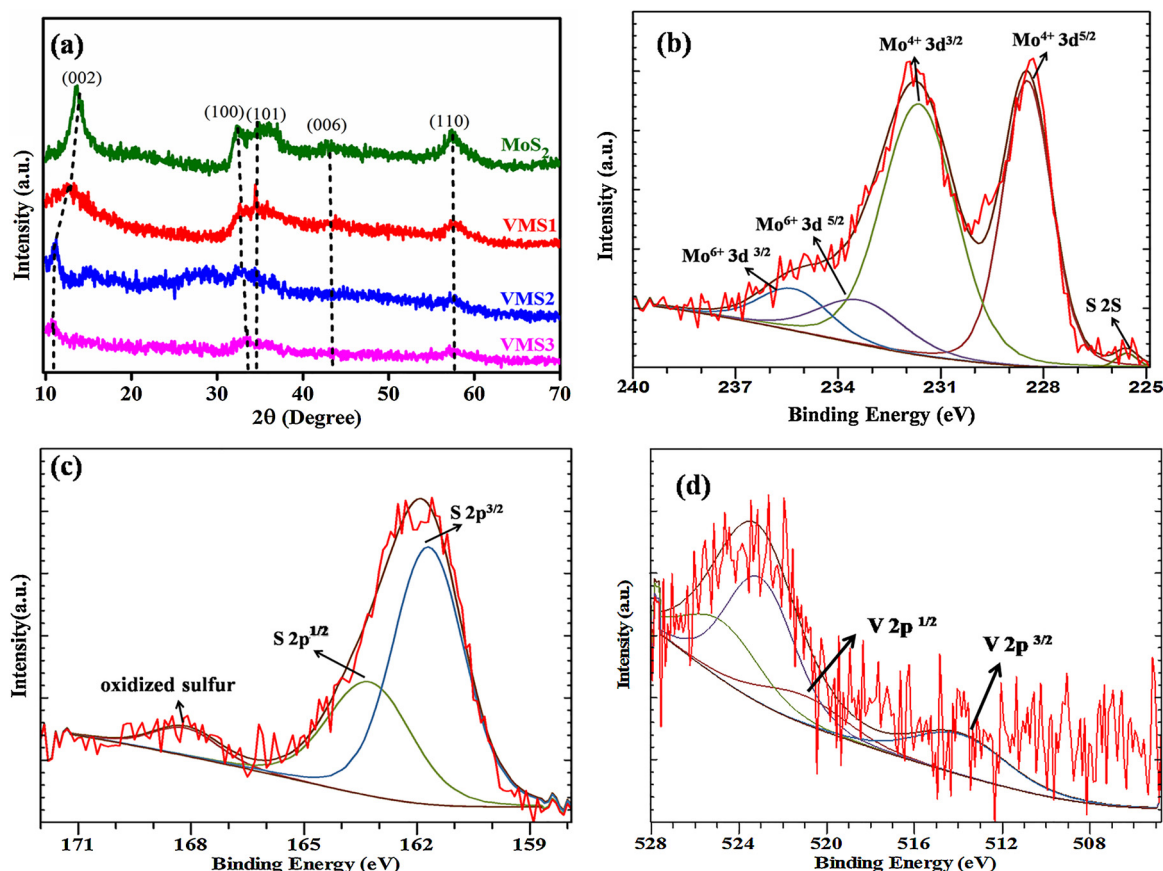


Fig. 3. a) XRD patterns of MoS<sub>2</sub>, VMS1, VMS2 and VMS3; deconvoluted depth profile of VMS2 for b) Mo3d, c) S 2p and d) V 2p.

**Table 2**

Atomic percentage of S, Mo and V obtained from XPS survey spectra analysis along with corresponding chemical composition.

Material	At% of S	At% of Mo	At% of V	Probable Composition
MoS <sub>2</sub>	69.61	30.39	0	MoS <sub>2</sub>
VMS1	65.37	32.98	1.65	V <sub>0.05</sub> Mo <sub>0.95</sub> S <sub>2</sub>
VMS2	65.33	31.82	2.84	V <sub>0.08</sub> Mo <sub>0.92</sub> S <sub>2</sub>
VMS3	64.15	31.61	4.24	V <sub>0.11</sub> Mo <sub>0.88</sub> S <sub>2</sub>

under solvothermal condition [38]. Fig. 3(d) shows the presence of V 2p<sup>1/2</sup> and V2p<sup>3/2</sup> in the deconvoluted V 2p spectra at -521.1 and -513.84 eV, respectively. Appearance of these two peaks confirmed the presence of V in +2 oxidation state [50]. Another two peaks at -525.9 and 523.7 eV appeared due to the formation of VO<sub>x</sub> with variable oxidation state (+4 and +5) of V. The V2p<sup>1/2</sup> signals (at higher binding energy region close to O1s peak) of VO<sub>x</sub> were taken into account for subtracting the background at higher binding energy region close to O1s. The intensity of V2p<sup>3/2</sup> is negligible as compared to the V2p<sup>1/2</sup> of VO<sub>x</sub> designating peaks since O1s peak is not included in the range for background determination [51].

### 3.5. Optical properties / UV–vis absorption spectrum analysis

UV-Vis spectroscopy was performed in 1:1 water-ethanol solvent to understand the optical behaviour. Fig. S3 (a) of supporting information represents the UV–vis absorption spectra of MoS<sub>2</sub> and VMS2. The 2nd derivative (inset of Fig S3(a)) of two spectra noticeably indicated that there is minor shift of peak positions in case of VMS2. The Band gap energy value obtained from the Tauc plot by extrapolating the straight line to the X-axis intercept is represented in Fig S3(b). Results indicated that VMS2 (2.29 eV) showed narrow band gap as compared to MoS<sub>2</sub>

(2.46 eV). Lower energy gap facilitated the charge transfer process of VMS2 compared to the pure MoS<sub>2</sub> for HER process. So, band gap energy decreased after V- doping in MoS<sub>2</sub> resulting significant improvement in electrocatalytic behaviour.

### 3.6. ICP-AES analysis

ICP-AES was performed to get the percentage of V, Mo and S in VMSd. The obtained data shows that the percentage of S is ~2 times higher than that of Mo in all VMSd samples (Table S1). The V content is very low as compared to both Mo and S. The ICP-AES revealed the accurate atomic ratios of Mo/S as 1:1.93 (VMS1), 1:1.87 (VMS2) and 1:2.02 (VMS3), respectively. All these observations suggested that the probable composition of VMSd is V<sub>0.0348</sub>Mo<sub>0.965</sub>S<sub>2</sub>, V<sub>0.08</sub>Mo<sub>0.919</sub>S<sub>2</sub>, and V<sub>0.107</sub>Mo<sub>0.892</sub>S<sub>2</sub>, respectively.

### 3.7. Electrochemical analysis

Electrochemical characterization was carried out to attain the knowledge on HER activity in acidic and alkaline mediums. LSV was performed in 0.5 M H<sub>2</sub>SO<sub>4</sub> for all the prepared materials and Pt/C. pH of the acidic electrolyte was calculated from current vs potential plot, taking Pt as working electrode. The calculated pH was found to be -1.067 (Supporting information for the calculation). A mean value of -0.257 V was obtained from the cathodic and anodic linear sweep at zero current response (Shown in Fig. S4). From polarization curves (as shown in Fig. 4a), it was observed that VMS2 had the lowest overpotential value among all the doped compositions along with pure MoS<sub>2</sub>. However, Pt/C considered as the superior material for electrocatalytic HER. It was observed that VMS2 required ~194 mV overpotential (η<sub>10</sub>) to achieve benchmarking current density of 10 mA cm<sup>-2</sup> which was lower than that of VMS1 (having η<sub>10</sub> ≈ 222 mV), VMS3

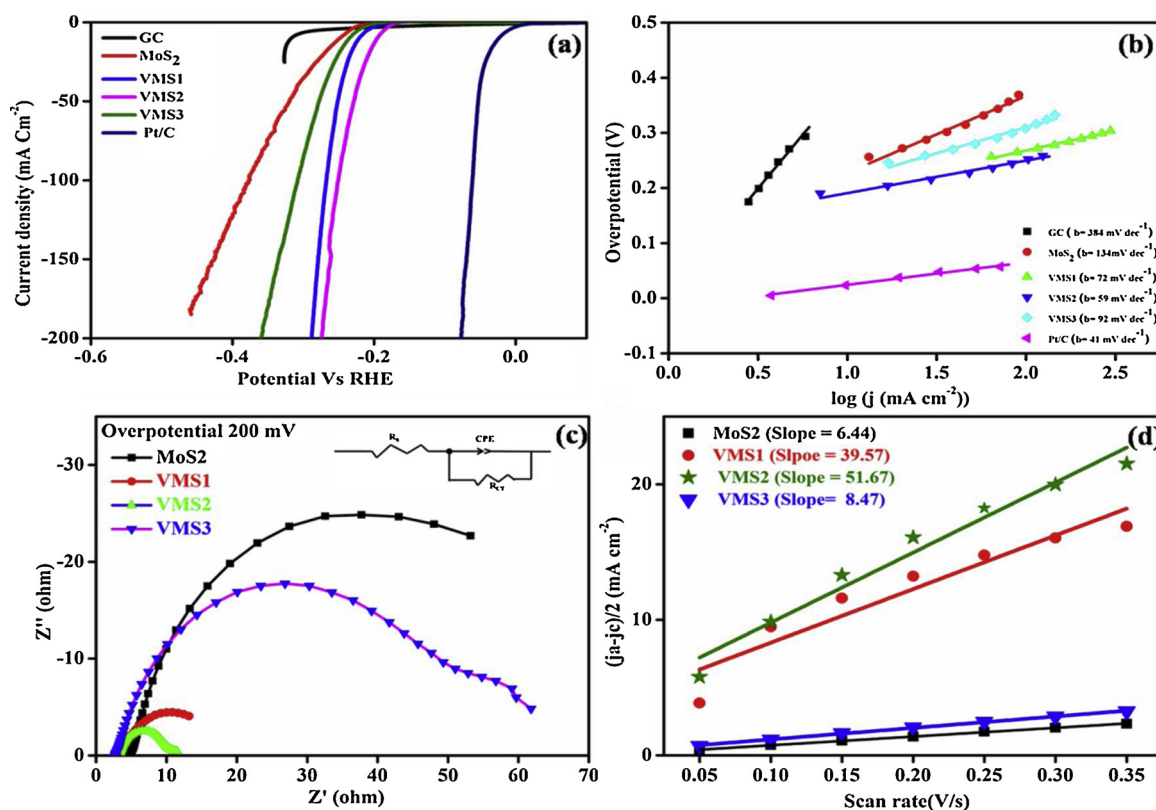
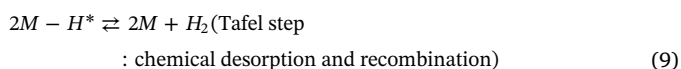
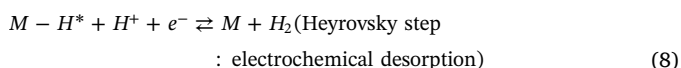
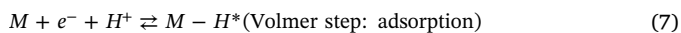


Fig. 4. a) HER polarization curve (iR corrected) of MoS<sub>2</sub>, VMS1, VMS2, VMS3, GC and Pt/C, b) Corresponding Tafel plots, c) Nyquist plots of MoS<sub>2</sub>, VMS1, VMS2, VMS3 at 200 mV over potential, d) Electrochemical active surface area measurements of MoS<sub>2</sub>, VMS1, VMS2 and VMS3 [0.5 M H<sub>2</sub>SO<sub>4</sub>].

(having  $\eta_{10} \approx 238$  mV) and MoS<sub>2</sub> (having  $\eta_{10} \approx 252$  mV). The obtained results are comparable with the previously reported values for non-noble metal-based electro-catalyst for HER activity in acidic condition [52,53]. Chen et al. reported VS<sub>2</sub>@MoS<sub>2</sub> nanoflowers with a low overpotential of 177 mV at 10 mA cm<sup>-2</sup> current density in 0.5 M H<sub>2</sub>SO<sub>4</sub> electrolyte. This study has analogous electrocatalytic HER activity with the present work [54]. Judicious doping of V effectively increased the electro-catalytic activity of MoS<sub>2</sub> due to the enhanced carrier concentration and in-plane conductivity which was reflected in VMS2 [45]. The kinetics study and mechanistic pathway for HER in acidic medium were examined using Tafel plots of all VMSd composition along with Pt/C and pure MoS<sub>2</sub> (depicted in Fig. 4b). VMS2 had the lowest Tafel slope value of  $\sim 59$  mV dec<sup>-1</sup> as compared to VMS1 ( $\sim 72$  mV dec<sup>-1</sup>) and VMS3 ( $\sim 92$  mV dec<sup>-1</sup>). The Tafel slope values for VMS1 and VMS3 were found to be intermediate between that for MoS<sub>2</sub> and VMS2. Smallest Tafel value corresponds to the increased reaction rate with growing potential confirming the superior electro-catalytic activity towards HER. The lower Tafel slope value signified a faster kinetics for VMS2 suggesting it to be better HER catalyst than the other one. Three elementary reaction steps are observed in HER electro-catalytic process, these are primary discharge step and consecutive steps of desorption or recombination [55]:



Tafel slope is inherent intrinsic property of an electro-catalyst allied with the mechanism. From the Tafel slope analysis, VMS2 followed the Volmer-Heyrovsky mechanistic pathway where Heyrovsky step is the

rate determining step. In brief, at first H<sup>+</sup> gets absorbed onto the surface of the electrode which later produces gaseous hydrogen through electrochemical desorption step. Higher reaction rate reflected from the Tafel slope value of VMS2, also supported by the polarization curve. Successive V-doping effectively increased the electro-catalytic activity of pure MoS<sub>2</sub>. But the controlled doping is highly efficient for HER due to its most favourable and stable chemical state as well as physical modification. Furthermore, the lower Tafel value and conspicuously low overpotential were required to achieve a fixed current density which was comparable with the recently reported state-of-the-art catalysts reported in the literature (Table S2). In order to understand the electrode-electrolyte interface chemistry, EIS study was performed at fixed overpotential of 200 mV. Fig. 4c demonstrated the Nyquist Plot of the studied electrodes. Calculated  $R_{ct}$  values, obtained from Z View software, were 68, 48.9, 8.01, and 17.79  $\Omega$  for MoS<sub>2</sub>, VMS3, VMS2 and VMS1, respectively (as presented in Table S4).  $R_{ct}$  value clearly exhibited faster charge transfer ability of VMS2 as compared to others due to its modified electronic properties. Difference in electronegativity of the host molybdenum active site and guest V leads to the modification of electronic properties of VMSd through heteroatom doping. The charge transfer between the host and guest facilitated to modify the charge density around the nanostructure which effectively improved electrical conductivity resulting enhanced catalytic activity towards HER [56–59]. ECSA was calculated from the  $C_s$  and  $C_{dl}$  values obtained from the CV plots to exactly understand the origin behind the increasing electro-catalytic activity of VMSd (depicted in Fig. S5). Calculated  $C_{dl}$  values of MoS<sub>2</sub>, VMS1, VMS2, VMS3 were 6.44, 39.57, 51.67, and 8.47 mF cm<sup>-2</sup>, respectively (demonstrated in Fig. 4d). Calculated ECSA value were  $\sim 184$ , 1130, 1476 and 242 cm<sup>2</sup> for MoS<sub>2</sub>, VMS1, VMS2 and VMS3, respectively. Roughness factor was also calculated and summarized in Table S6. At a fixed overpotential with increasing ECSA value, current density also increased (see in Fig. S 6a, b). It may be due to the enhanced surface active sites after V-doping which



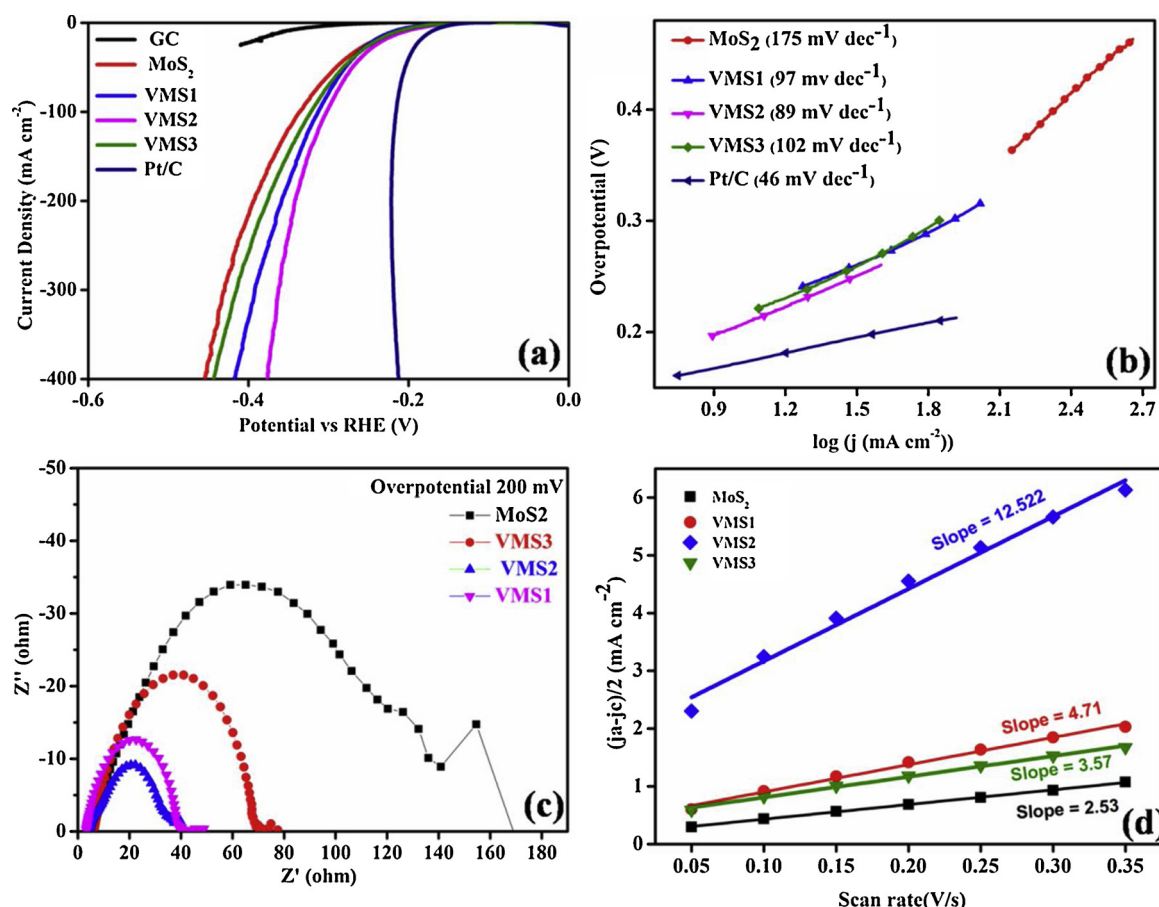
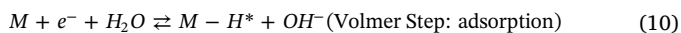


Fig. 5. a) HER polarization curve (iR corrected) of MoS<sub>2</sub>, VMS1, VMS2, VMS3, GC and Pt/C, b) Corresponding Tafel plots, c) Nyquist plots of MoS<sub>2</sub>, VMS1, VMS2, VMS3 at 200 mV over potential, d) Electrochemical active surface area measurements of MoS<sub>2</sub>, VMS1, VMS2 and VMS3 [1 M KOH medium].

activated the inert basal planes by introducing defects [59]. However, little energy difference between defect sites and valence band maxima enhanced the activity of valence electrons towards HER [60]. The defect sites enhanced the active sites of molybdenum atom. Electro-catalytic performance of MoS<sub>2</sub> effectively enhanced through controlled V-doping, supported by the ECSA study. LSV of all materials were performed to understand the HER activity in 1 M KOH solution. The polarization curve (as shown in Fig. 5a) revealed that Pt/C required low overpotential at 10 mA cm<sup>-2</sup> as compared to other materials. VMS2 showed superior catalytic property due to lower overpotential value of -206 mV at 10 mA cm<sup>-2</sup>, slightly lower than those of VMS1, VMS3 and MoS<sub>2</sub> (depicted in the Fig. 5a). Overpotential values of -303, 314, 323 and 335 mV were needed to achieve a current density of 100 mA cm<sup>-2</sup> for VMS2, VMS1, VMS3 and MoS<sub>2</sub>, respectively. Tafel slope analysis in alkaline pH was carried out to understand the HER mechanism involved for VMSd and MoS<sub>2</sub>.

The corresponding Tafel slope values for MoS<sub>2</sub>, VMS1, VMS2 and VMS3 were derived to be -175, 97, 89 and 102 mV dec<sup>-1</sup>, respectively (as depicted in Fig. 5b). VMS2 displayed the lowest Tafel slope value suggesting it to be superior electro-catalyst among those materials. However, detailed analysis of the Tafel slope value predicted the rate determining step to be the Heyrovsky step. According to Heyrovsky step, electrochemical desorption step is the rate determining step followed by the Volmer step (H<sup>+</sup> ion gets absorbed on the surface of the working electrode).



It is seen that the VMS2 is a promising electro-catalyst for HER in alkaline medium and its performance was comparable to those of the materials recently reported in literature (as shown in the Table S3).

EIS analysis was performed for better understanding of the HER kinetics in basic medium. Therefore, it was executed at a fixed potential of 200 mV (depicted in Fig. 5c). Corresponding charge transfer ability at the electrode-electrolyte interface was speculated from the Nyquist Plot. R<sub>ct</sub> value obtained from the Nyquist plot were found to be 125, 37, 30.5, and 64.08 mV dec<sup>-1</sup> for MoS<sub>2</sub>, VMS1, VMS2 and VMS3, respectively (as shown in Table S5). The C<sub>dl</sub> values (obtained from Fig. 5d) were also measured from the CV study in 1 M KOH solution (as shown in Fig. S6). The corresponding ECSA and RF values were calculated using Eq. (3) and summarized in Table S7. Absolute Current density vs ECSA plot at a fixed overpotential showed the enhancement of absolute current density with growing ECSA value (as shown in Fig. S7c, d). Due to higher catalytic active surface area, gaseous hydrogen production through Volmer-Heyrovsky mechanism got enhanced which was also reflected in the ECSA value of VMS2.

In summary, the experimental reaction rate of the HER in acidic medium was faster than that of alkaline solution. An additional amount of overpotential is required for alkaline medium to reach the fixed current density (j<sub>0</sub>) as compared to acidic one. Larger amount of hydrogen binding energy is necessary for hydrogen adsorption due to extra water dissociation step or entropic barrier for water dipole formation. The sluggish kinetics of HER in alkaline medium is due to the lesser concentration of H<sup>+</sup> ions and difficulty in the formation of M-H\*. Higher amount of energy barrier is generated due to the additional water association involved in alkaline medium [61–64]. So, HER is more feasible and progress faster in acidic medium as compared to the basic medium owing to different mechanistic pathways associated with the two different medium.

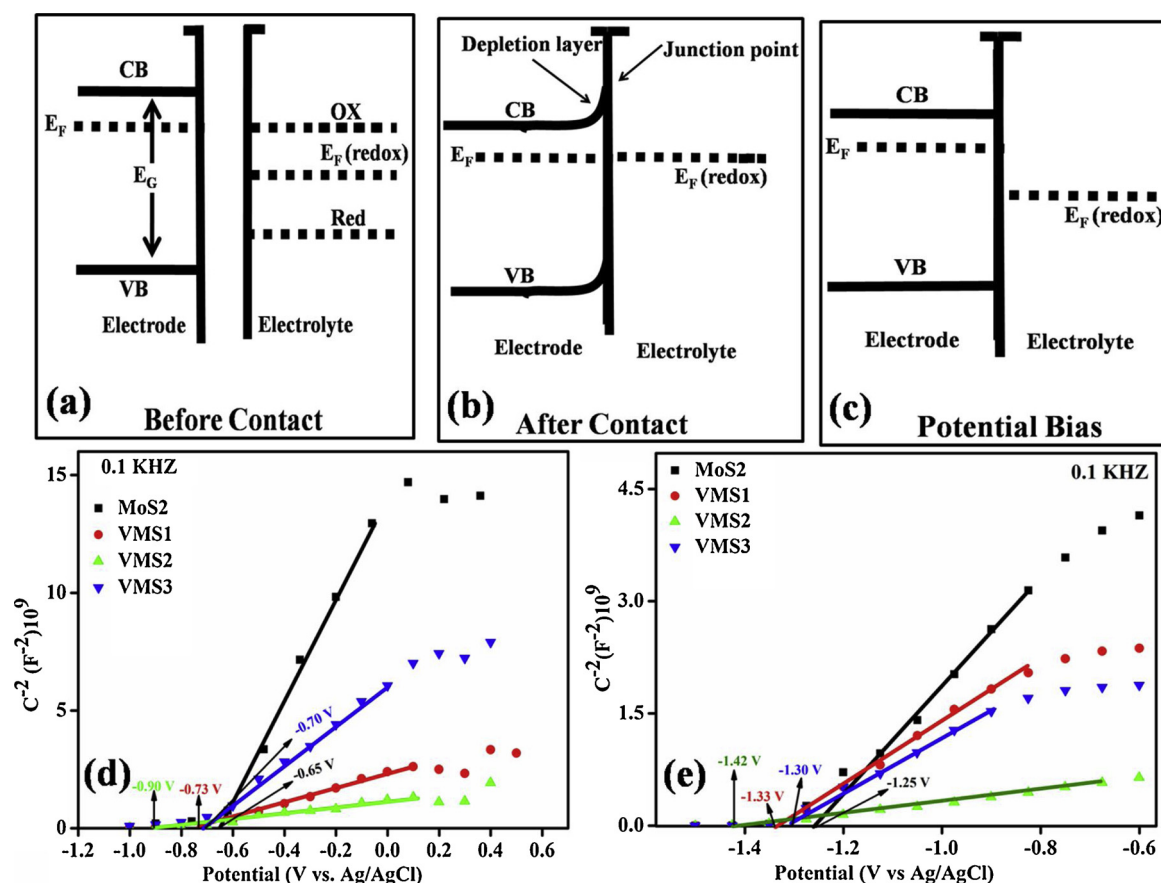


Fig. 6. Conduction and Valence band behaviour in electrode and electrolyte interface: a) before contact, b) after contact, c) under potential bias d, e) Mott-Schottky plot measured in 0.1 KHz in both 0.5 M  $\text{H}_2\text{SO}_4$  and 1 M KOH respectively for  $\text{MoS}_2$ , VMS1, VMS2 and VMS3.

### 3.8. Mott-Schottky analysis

The effect of V-doping on the electro-catalytic properties of  $\text{MoS}_2$  was investigated at the interface of electrolyte-electrode in acidic and basic medium using Mott-Schottky analysis (Fig. 6 d,e). A comparable potential difference should be present at the interface of electrode and electrolyte. The potential difference was calculated from the redox potential of the electrolyte and Fermi level of the electrode material. The charge transfer ability of the doped materials and pure  $\text{MoS}_2$  were different due to their different valence and conduction band position [65,66]. A minor potential difference is always present in between the Fermi level of electrode and electrolyte (Fig. 6a). As the electrodes come in contact with the electrolyte, these two potential systems tries to maintain equilibrium to successfully transfer charge from one potential region to another. So, after effective transfer of charge between electrode and electrolyte interface, equilibrium position should be reached (Fig. 6b). Pure  $\text{MoS}_2$  behaved as n-type semiconductor as negative slope was obtained from Mott-Schottky plot (as shown in Fig. 6 d, e). After doping with V,  $\text{MoS}_2$  retained its n-type nature as evidenced from the negative slope. The n-type semiconductor and electrolyte attain equilibrium through the transfer of electron from electrode to electrolyte so that Fermi level of both the phase is comparable. This makes the electrode charging positively (space charge region) which was counter balanced by electrolyte sheet of charge. This phenomenon caused the separation of electrode and redox couple Fermi level, was resulting a band bending of electrode (Fig. 6b). A semiconductor electrode and electrolyte junction was in flat band potential when there was no band bending at a certain applied potential (Fig. 6c). Corresponding flat band potential and donor density of the electrode were calculated from Mott-Schottky plot using the following equations [67]:

$$\frac{1}{C^2} = \frac{2}{N_D \epsilon \epsilon_0 e} \left( E - E - \frac{KT}{e} \right) \quad (11)$$

$$N_D = \frac{2}{\epsilon \epsilon_0 e} \left( \frac{dE}{d\left(\frac{1}{C^2}\right)} \right) \quad (12)$$

where,  $\epsilon$ ,  $\epsilon_0$ ,  $e$ ,  $N_D$ ,  $E_{FB}$ ,  $K$ ,  $T$  are dielectric constant of the materials, permittivity of the free space, electronic charge, number of donor density, flat band potential, Boltzmann constant and absolute temperature, respectively. Mott-Schottky plot clearly confirmed that all VMSd composition act as n-type, as negative slope obtained from the plot depicted in Fig. 6d. Moreover, for conventional n-type material, doped element has at least one additional electron than the acceptor. The flat band potential in acidic medium can be measured from the extrapolation of the linear fitted curve up to the X-axis at point  $1/C^2 = 0$ . The donor density was determined from the slope obtained from the linear fitted curve depicted in Fig. 6d. The calculated flat band potentials were -0.65, -0.73, -0.90 and -0.70 V for  $\text{MoS}_2$ , VMS1, VMS2, VMS3, respectively. Higher negative flat band potential is due to the improved donor density [67]. VMS2 having highest negative flat band potential than the others confirmed its greater charge transfer ability. The catalytic activity enhanced subsequently with increasing charge transfer ability. Hence, VMS2 performed as a superior electro-catalyst towards HER in acidic medium. The corresponding donor density determined from Eq. (12) is summarized in Table S8. Higher the donor density value higher would be the charge transfer ability was resulting a improved catalytic activity towards HER. The enhanced donor density also causes higher conductivity of doped materials which is essential for electrocatalysis [68]. Calculated Mott-Schottky data supported all the electrochemical results towards HER. Another interesting finding from



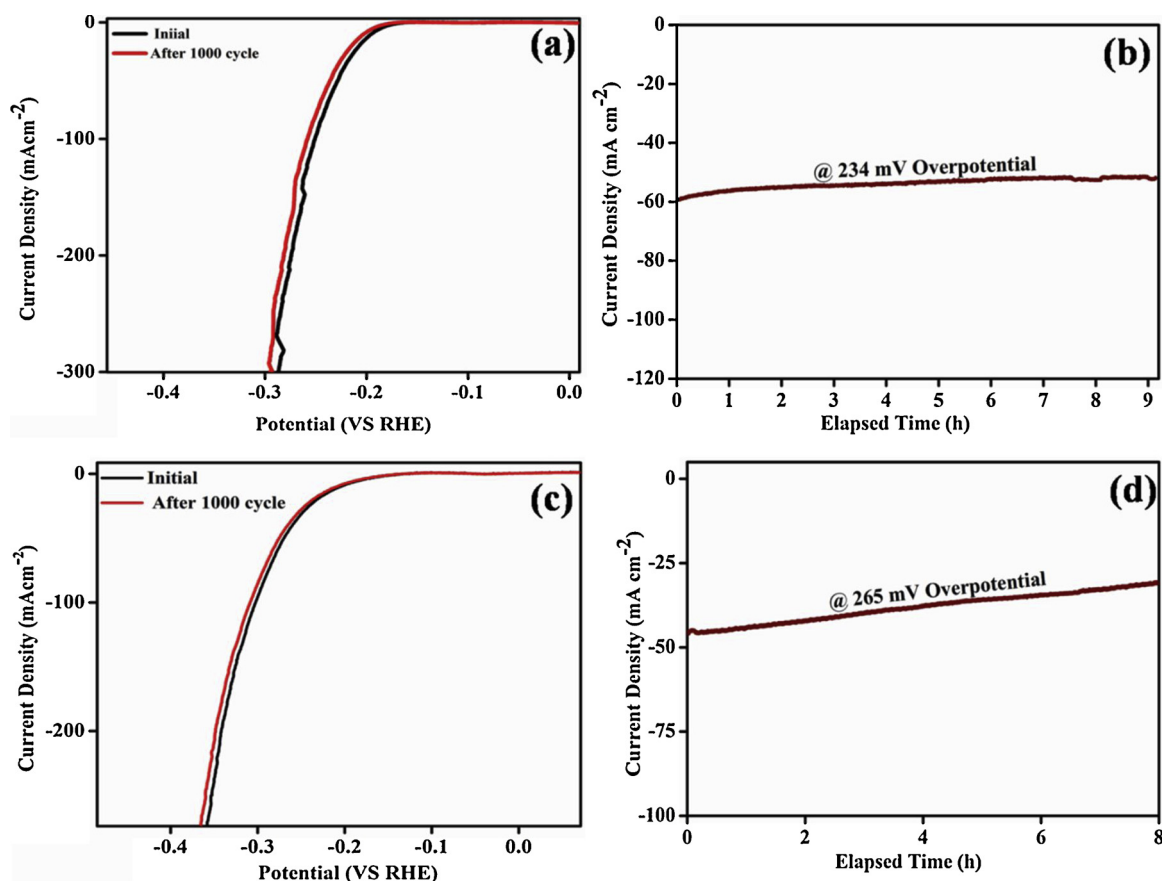


Fig. 7. a, c) HER Polarization curve of VMS2 before and after 1000 cycle at a scan rate of  $10 \text{ mV s}^{-1}$  in  $0.5 \text{ M H}_2\text{SO}_4$  and  $1 \text{ M KOH}$  respectively. b) Chronoamperometric curve of VMS2 at  $234 \text{ mV}$  for  $9 \text{ h}$  in  $0.5 \text{ M H}_2\text{SO}_4$ , d) Chronoamperometric curve of VMS2  $265 \text{ mV}$  for  $8 \text{ h}$  in  $1 \text{ M KOH}$ .

the Mott-Schottky analysis was that V ion doping retained the n-type property of MoS<sub>2</sub> and simultaneously decreased its  $\text{d}y/\text{d}x$  value. In MoS<sub>2</sub>, Mo is present as  $\text{Mo}^{4+}$  state ( $\text{d}^2$  system). The doped V should be present in  $\text{V}^{2+}$  state ( $\text{d}^3$  system) to maintain n-type property, as it has one electron extra than  $\text{Mo}^{4+}$  ion, which support the conventional n-type material. The ionic size of V (II) is  $92 \text{ pm}$  much higher than molybdenum (IV) of value  $79 \text{ pm}$  [69]. Moreover the other achievable oxidation state of V atom has lower ionic size ( $\text{V}^{3+} = 78 \text{ pm}$ ,  $\text{V}^{4+} = 72 \text{ pm}$ ,  $\text{V}^{5+} = 68 \text{ pm}$ ) compared to molybdenum in  $+4$  oxidation state. From XRD plot we observed that on V-doping, (002) plane shifted towards lower angle, which also supported the presence of V as  $+2$  state in MoS<sub>2</sub>. The shift of (002) plane towards lower  $\theta$  value happened due to larger size dopant presence in MoS<sub>2</sub> crystal lattice. Both Mott-Schottky plot and XRD analysis support the presence of  $\text{V}^{2+}$  ion in MoS<sub>2</sub> nanoflower.

The Mott-Schottky analysis was performed in basic medium at same frequency as that in acidic medium. The flat band potential [from Fig. 6e] was  $-1.25$ ,  $-1.33$ ,  $-1.42$  and  $-1.30 \text{ V}$  for MoS<sub>2</sub>, VMS1, VMS2 and VMS3, respectively. The corresponding donor density was calculated and summarized in Table S9. The flat band potential value increased with increasing pH. With increase of pH value by one unit, flat band potential value elevated (negative value) at a rate in between  $-40 \text{ mV/pH}$  to  $-59 \text{ mV/pH}$  [70]. The band edges at the surface shifted towards higher energies with increasing pH value. So at higher pH value, electrode potential value shifted towards more cathodic region. Hence, the flat band potential value was higher in basic medium as compared to the acidic medium [71]. As a result, the electrically active surface state density was higher in acidic medium (lower pH) which promoted the catalytic activity of VMS2 in acidic medium compared to basic one [72]. This phenomenon supported the overpotential values obtained in both acidic and basic medium at a fixed current density.

### 3.9. Stability

Apart from good catalytic property of VMS2, another important criterion for practical application is the durability. More than 1000 CV scans were performed within a potential range of  $0.1$  to  $-0.4 \text{ V}$  (vs. RHE) with a scan rate of  $100 \text{ mV s}^{-1}$  in both  $0.5 \text{ M H}_2\text{SO}_4$  and  $1 \text{ M KOH}$ , to probe the stability of the material. Final LSV curve was also plotted in both the medium (depicted in Fig. 7a, c) which was almost comparable with the initial one. No significant change in current density was observed after 1000 CV scan.

Chronoamperometry was performed for  $\sim 9 \text{ h}$  at  $234 \text{ mV}$  overpotential in acidic medium (Fig. 7b) to check the long-term functional durability. A similar study was performed at an overpotential of  $265 \text{ mV}$  for  $\sim 8 \text{ h}$  to check the durability in basic medium (Fig. 7d). All the studies clearly concluded that VMS2 could be used as HER electrocatalyst in both acidic and basic medium for a long period of time.

## 4. Conclusions

In summary, VMSd nanoflowers were synthesized by facile one-step solvothermal procedure. Structure as well as electronic environment synergistically enhanced HER activity in both acidic and basic medium which was confirmed from the fact that a low overpotential was required to achieve the benchmarking current density. After incorporation of V into the MoS<sub>2</sub> nanoflowers, the active surface area increased enormously which enhanced the catalytic performance towards HER. Moreover, optimized incorporation substantially reduced the band gap, enhancing the charge transferability and exhibited a superior HER activity. The physio-chemical analysis suggested that V atom was incorporated symmetrically in MoS<sub>2</sub> nanoflower. Thorough study of polarization curve vividly concluded that V was doped successfully and it

helped in improving the electrocatalytic activity towards HER. Mott-Schottky plot explained that on V-doping, the flat band potential changed. The change in  $E_F$ , effected the charge transfer property and donor density significantly and as a result the activity towards HER performance got enhanced. Long-term stability in both acidic and basic medium was achieved, which suggested that the optimized V doped  $\text{MoS}_2$  catalyst could be a subsidiary alternative for Pt based HER electrocatalysts. Therefore, to effectively modify the electrocatalytic activity towards HER, transition metal atom doping on TMDS via facile one-step procedure, is an efficient strategy.

## Acknowledgements

The authors are also thankful to the Director of CSIR-CMERI, Durgapur.

## Appendix A. Supplementary data

Supplementary material related to this article can be found, in the online version, at doi:<https://doi.org/10.1016/j.apcatb.2019.04.028>.

## References

- [1] S. Chu, A. Majumdar, Opportunities and challenges for a sustainable energy future, *Nature* 488 (2012) 294–303.
- [2] J. Yan, Y. Zheng, M. Jaroniec, S.Z. Qiao, Design of electrocatalysts for oxygen- and hydrogen-involving energy conversion reactions, *Chem. Soc. Rev.* 44 (2015) 2060–2086.
- [3] M.S. Dresselhaus, I.L. Thomas, Alternative energy technologies, *Nature* 414 (2001) 332–337.
- [4] J. Chow, R.J. Kopp, P.R. Portney, Energy resources and global development, *Science* 302 (2003) 1528–1531.
- [5] Y. Wang, D. Yan, S.E. Hankari, Y. Zou, S. Wang, Recent progress on layered double hydroxides and their derivatives for electrocatalytic water splitting, *Adv. Sci.* 5 (2018) 1800064.
- [6] S. Yi, Y. Zhou, D.R. Yang, W.X. Xe, C. Wang, F.B. Wang, J.J. Xu, X.H. Xia, H.Y. Chen, Energy level engineering of  $\text{MoS}_2$  by transition-metal doping for accelerating hydrogen evolution reaction, *J. Am. Chem. Soc.* 139 (2017) 15479–15485.
- [7] Y. Zeng, Y. Wang, G. Huang, C. Chen, L. Huang, R. Chen, S. Wang, Porous CoP nanosheets converted from layered double hydroxides with superior electrochemical activity for hydrogen evolution reaction at wide pH range, *Chem. Commun. (Camb.)* 54 (2018) 1465–1468.
- [8] X. Li, H. Zhu, Two-dimensional  $\text{MoS}_2$ : properties, preparation, and applications, *J. Mater. Sci.* 1 (2015) 33–44.
- [9] X. Sun, J. Dai, Y. Guo, C. Wu, F. Hu, J. Zhao, X. Zeng, Y. Xie, Semimetallic molybdenum disulfide ultrathin nanosheets as an efficient electrocatalyst for hydrogen evolution, *Nanoscale* 6 (2016) 8359–8367.
- [10] H. Tang, S.R. Morrison, Optimization of the anisotropy of composite  $\text{MoS}_2$  film, *Thin Solid Films* 227 (1993) 90–94.
- [11] T.H.M. Lau, X.W. Lu, J. Kulhavy, S. Wu, L. Lu, T.S. Wu, R. Kato, J.S. Foord, Y.L. Soo, K. Suenagad, S.C.E. Tsang, Transition metal atom doping of the basal plane of  $\text{MoS}_2$  monolayer nanosheets for electrochemical hydrogen evolution, *Chem. Sci.* 9 (2018) 4769–4776.
- [12] J. Kibsgaard, Z. Chen, B.N. Reinecke, T.F. Jaramillo, Engineering the surface structure of  $\text{MoS}_2$  to preferentially expose active edge sites for electrocatalysis, *Nat. Mater.* 11 (2012) 963–969.
- [13] H. Wang, H. Yuan, S.S. Hong, Y. Li, Y. Cui, Physical and chemical tuning of two-dimensional transition metal dichalcogenides, *Chem. Soc. Rev.* 44 (2015) 2664–2680.
- [14] B. Hinnemann, P.G. Moses, J. Bonde, K.P. Jørgensen, J.H. Nielsen, S. Hørch, I.B. Chorkendorff, J.K. Nørskov, Biomimetic hydrogen evolution:  $\text{MoS}_2$  nanoparticles as catalyst for hydrogen evolution, *J. Am. Chem. Soc.* 127 (2005) 5308–5309.
- [15] S. Li, S. Wang, M.M. Salamone, A.W. Robertson, S. Nayak, H. Kim, S.C.E. Tsang, M. Pasta, J.H. Warner, Edge-enriched 2D  $\text{MoS}_2$  thin films grown by chemical vapor deposition for enhanced catalytic performance, *ACS Catal.* 7 (2017) 877–886.
- [16] G. Ye, Y. Gong, J. Lin, B. Li, Y. He, S.T. Pantelides, W. Zhou, R. Vajtai, P.M. Ajayan, Defects engineered monolayer  $\text{MoS}_2$  for improved hydrogen evolution reaction, *Nano Lett.* 16 (2016) 1097–1103.
- [17] C. Tsai, F.A. Pedersen, J.K. Nørskov, Tuning the  $\text{MoS}_2$  edge-site activity for hydrogen evolution via support interactions, *Nano Lett.* 14 (2014) 1381–1387.
- [18] X. Huang, Z. Zeng, S. Bao, M. Wang, X. Qi, Z. Fan, H. Zhang, Solution-phase epitaxial growth of noble metal nanostructures on dispersible single-layer molybdenum disulfide nanosheets, *Nat. Commun.* 4 (2013) 1444.
- [19] D. Kong, H. Wang, J.J. Cha, M. Pasta, K. Koski, J.J. Yao, Y. Cui, Synthesis of  $\text{MoS}_2$  and  $\text{MoSe}_2$  films with vertically aligned layers, *Nano Lett.* 13 (2013) 1341–1347.
- [20] J. Kim, S. Byun, A.J. Smith, J. Yu, J. Huang, Enhanced electrocatalytic properties of transition-metal dichalcogenides sheets by spontaneous gold nanoparticle decoration, *J. Phys. Chem. Lett.* 4 (2013) 1227–1232.
- [21] J. Ye, W. Chen, S. Xu, Z. Yu, S. Hou, Synthesis of Co-doped  $\text{MoS}_2$ /graphene hybrids as an enhanced electrocatalyst for hydrogen evolution reaction, *RSC Adv.* 6 (2016) 104925–104932.
- [22] C. Huang, Y. Jin, W. Wang, L. Tang, C. Song, F. Xiu, Manganese and chromium doping in atomically thin  $\text{MoS}_2$ , *J. Semicond.* 38 (2017) 033004.
- [23] K. Zhang, S. Feng, J. Wang, A. Azcatl, N. Lu, R. Addou, N. Wan, C. Zhou, J. Lerach, V. Bojan, M.J. Kim, L.Q. Chen, R.M. Wallace, M. Terrones, J. Zhu, J.A. Robinson, Manganese doping of monolayer  $\text{MoS}_2$ : the substrate is critical, *Nano Lett.* 15 (2015) 6586–6591.
- [24] X. Sun, J. Huo, Y. Yang, L. Xu, S. Wang, The  $\text{Co}_3\text{O}_4$  nanosheet array as support for  $\text{MoS}_2$  as highly efficient electrocatalysts for hydrogen evolution reaction, *J. Energy Chem.* 26 (2017) 1136–1139.
- [25] D. Kiriya, M. Tosun, P. Zhao, J.S. Kang, A. Jave, Air-stable surface charge transfer doping of  $\text{MoS}_2$  by benzyl viologen, *J. Am. Chem. Soc.* 136 (2014) 7853–7856.
- [26] Y. Li, H. Wang, L. Xie, Y. Liang, G. Hong, H. Dai,  $\text{MoS}_2$  nanoparticles grown on graphene: an advanced catalyst for hydrogen evolution reaction, *J. Am. Chem. Soc.* 133 (2011) 7296–7299.
- [27] J. Xie, H. Zhang, S. Li, R. Wang, X. Sun, M. Zhou, J. Zhou, X.W. (David) Lou, Y. Xie, Defect-rich  $\text{MoS}_2$  ultrathin nanosheets with additional active edge sites for enhanced electrocatalytic hydrogen evolution, *Adv. Mater.* 25 (2013) 5807–5813.
- [28] M.A. Lukowski, A.S. Daniel, F. Meng, A. Forticaux, L. Li, S. Jin, Enhanced hydrogen evolution catalysis from chemically exfoliated metallic  $\text{MoS}_2$  nanosheets, *J. Am. Chem. Soc.* 135 (2013) 10274–10277.
- [29] X. Chia, A. Ambrosi, D. Sedmidubsky, Z. Sofer, M. Pumer, Precise tuning of the charge transfer kinetics and catalytic properties of  $\text{MoS}_2$  materials via electrochemical methods, *Chem. Eur. J.* 20 (2014) 17426–17432.
- [30] S. Shin, Z. Jin, D.H. Kwon, R. Bose, Y.S. Min, High turnover frequency of hydrogen evolution reaction on amorphous  $\text{MoS}_2$  thin film directly grown by atomic layer deposition, *Langmuir* 31 (2015) 1196–1202.
- [31] D. Wanga, X. Zhang, Y. Shena, Z. Wua, Ni-doped  $\text{MoS}_2$  nanoparticles as highly active hydrogen evolution electrocatalysts, *RSC Adv.* 6 (2016) 16656–16661.
- [32] C. Yelgel, Ö.C. Yelgel, O. Gülsere, Structural and electronic properties of  $\text{MoS}_2$ ,  $\text{WS}_2$ , and  $\text{WS}_2/\text{MoS}_2$  heterostructures encapsulated with hexagonal boron nitride monolayers, *J. Appl. Phys.* 122 (2017) 065303.
- [33] G. Seifert, H. Terrones, M. Terrones, G. Jungnickel, T. Frauenheim, Structure and electronic properties of  $\text{MoS}_2$  nanotubes, *Phys. Rev. Lett.* 85 (2000) 146.
- [34] A. Boochani, V. Somaye, The vanadium effect on electronic and optical response of  $\text{MoS}_2$  graphene-like: using DFT, *Silicon* (2018) 1–9, <https://doi.org/10.1007/s12633-018-9825-0>.
- [35] D. Yan, M.Z. Bazant, P.M. Biesheuvel, M.C. Pugh, F.P. Dawson, Theory of linear sweep voltammetry with diffuse charge: unsupported electrolytes, thin films, and leaky membranes, *Phys. Rev. E* 95 (2017) 033303.
- [36] Y. Qu, M. Yang, J. Chai, Z. Tang, M. Shao, C.T. Kwok, M. Yang, Z. Wang, D. Chua, S. Wang, Z. Lu, H. Pan, Facile synthesis of vanadium-doped  $\text{Ni}_3\text{S}_2$  nanowire arrays as active electrocatalyst for hydrogen evolution reaction, *ACS Appl. Mater. Interfaces* 9 (2017) 5959–5967.
- [37] A. Allagui, T.J. Freeborn, A.S. Elwakil, B.J. Maundy, Reevaluation of performance of electric double-layer capacitors from constant-current charge/discharge and cyclic voltammetry, *Sci. Rep.* 6 (2016) 38568.
- [38] S. Shit, S. Chhetri, W. Jang, N.C. Murmu, H. Koo, P. Samanta, T. Kuila, Cobalt Sulfide/Nickel sulfide heterostructure directly grown on nickel foam: an efficient and durable electrocatalyst for overall water splitting application, *ACS Appl. Mater. Interfaces* 10 (2018) 27712–27722.
- [39] C.C.L. McCrory, S. Jung, I.M. Ferrer, S.M. Chatman, J.C. Peters, T.F. Jaramillo, Benchmarking hydrogen evolving reaction and oxygen evolving reaction electrocatalysts for solar water splitting devices, *J. Am. Chem. Soc.* 137 (2005) 4347–4357.
- [40] C.C.L. McCrory, S. Jung, J.C. Peters, T.F. Jaramillo, Benchmarking heterogeneous electrocatalysts for the oxygen evolution reaction, *J. Am. Chem. Soc.* 135 (2013) 16977–16987.
- [41] S. Kalluri, K.H. Song, Z. Guo, A. Du, K. Konstantinov, H.K. Liu, S.X. Dou, Sodium and Lithium storage properties of spray-dried molybdenum disulfide-graphene hierarchical microspheres, *Sci. Rep.* 5 (2015) 11989.
- [42] W. Fu, F.H. Du, J. Su, X.H. Li, X. Wei, T.N. Ye, K.X. Wang, J.S. Chen, In situ catalytic growth of large-area multilayered graphene/ $\text{MoS}_2$  heterostructures, *Sci. Rep.* 4 (2014) 4673.
- [43] L. Yang, X. Cui, J. Zhang, K. Wang, M. Shen, S. Zeng, S.A. Dayeh, L. Feng, B. Xiang, Lattice strain effects on the optical properties of  $\text{MoS}_2$  nanosheets, *Sci. Rep.* 4 (2014) 5649.
- [44] R.D. Shannon, Revised effective ionic radii and systematic studies of interatomic distances in Halides and chalcogenides, *Acta Cryst.* 32 (1976) 751.
- [45] X. Sun, J. Dai, Y. Guo, C. Wu, F. Hu, J. Zhao, X. Zeng, Y. Xie, Semimetallic molybdenum disulfide ultrathin nanosheets as an efficient electrocatalyst for hydrogen evolution, *Nanoscale* 6 (2014) 8359–8367.
- [46] X. Wang, Y.P. Zhang, Z.Q. Chen, Effect of  $\text{MoO}_3$  constituents on the growth of  $\text{MoS}_2$  nanosheets by chemical vapor deposition, *Mater. Res. Express* 3 (2016) 065014.
- [47] J.C. Park, H. Song, Synthesis of polycrystalline  $\text{Mo}/\text{MoO}_x$  nanoflakes and their transformation to  $\text{MoO}_3$  and  $\text{MoS}_2$  nanoparticles, *Chem. Mater.* 19 (2007) 2706–2708.
- [48] L. Zhao, J. Jia, Z. Yang, J. Yu, A. Wang, Y. Sang, W. Zhou, H. Liu, One-step synthesis of  $\text{CdS}$  Nanoparticles/ $\text{MoS}_2$  nanosheets heterostructure on porous molybdenum sheet for enhanced photocatalytic  $\text{H}_2$  evolution, *Appl. Catal. B* 210 (2017) 290–296.
- [49] S. Shit, S. Chhetri, S. Bolar, N.C. Murmu, W. Jang, H. Koo, T. Kuila, Hierarchical cobalt sulfide @ molybdenum sulfide heterostructure as a bifunctional electrocatalyst towards overall water splitting, *Chem. Electrochem.* 6 (2018) 430–438.
- [50] M.C. Biesinger, L.W.M. Lau, A.R. Gerson, R.St.C. Smart, Resolving surface

- chemical states in XPS analysis of first row transition metals, oxides and hydroxides: Sc, Ti, V, Cu and Zn, *Appl. Surf. Sci.* 257 (2010) 887–898.
- [51] G. Silversmit, D. Depla, H. Poelman, G.B. Marin, R.D. Gryse, Determination of the V2p XPS binding energies for different vanadium oxidation states (V5+ to V0+), *J. Electron Spectros. Relat. Phenomena* 135 (2004) 167–175.
- [52] F.Z. Wang, M.J. Zheng, B. Zhang, C.Q. Zhu, Q. Li, L. Ma, W.Z. Shen, Ammonia intercalated flower-like MoS<sub>2</sub> nanosheet film as electrocatalyst for high efficient and stable hydrogen evolution, *Sci. Rep.* 6 (2016) 31092.
- [53] J.D. Benck, Z. Chen, L.Y. Kuritzky, A.J. Forman, T.F. Jaramillo, Amorphous molybdenum sulfide catalysts for electrochemical hydrogen production: insights into the origin of their catalytic activity, *ACS Catal.* 2 (2012) 1916–1923.
- [54] X. Chen, K. Yu, Y. Shen, Y. Feng, Z. Zhu, Synergistic effect of MoS<sub>2</sub> nanosheets and VS<sub>2</sub> for the hydrogen evolution reaction with enhanced humidity-sensing performance, *ACS Appl. Mater. Interfaces* 9 (2017) 42139–42148.
- [55] T. Shinagawa, A.T. Garcia-Esparza, K. Takanabe, Insight on Tafel slopes from a microkinetic analysis of aqueous electrocatalysis for energy conversion, *Sci. Rep.* 5 (2015) 13801.
- [56] S. Kouser, S.R. Lingampalli, P. Chithaiah, A. Roy, S. Saha, U.V. Waghmare, C.N.R. Rao, Extraordinary changes in the electronic structure and properties of CdS and ZnS by anionic substitution: cosubstitution of P and Cl in place of S<sup>2-</sup>, *Angew. Chem. Int. Ed.* 54 (2015) 8149–8153.
- [57] J. Duan, S. Chen, M. Jaroniec, S.Z. Qiao, Porous C<sub>3</sub>N<sub>4</sub> Nanolayers@N-Graphene films as catalyst electrodes for highly efficient hydrogen evolution, *ACS Nano* 9 (2015) 931–940.
- [58] Y. Pan, Y. Liu, Y. Lin, C. Liu, Metal doping effect of the M-Co2P/NCNTs (M = Fe, Ni, Cu) hydrogen evolution hybrid catalysts, *ACS Appl. Mater. Interfaces* 8 (2016) 13890–13901.
- [59] Y. Ouyang, C. Ling, Q. Chen, Z. Wang, L. Shi, J. Wang, Activating inert basal Planes of MoS<sub>2</sub> for hydrogen evolution reaction through the formation of different intrinsic defects, *Chem. Mater.* 28 (2016) 4390–4396.
- [60] M.D. Wales, L.B. Joos, W.A. Traylor, P. Pfromm, M. Reza, Composite catalytic tubular membranes for selective hydrogenation in three-phase systems, *Catal. Today* 268 (2016) 12–18.
- [61] T.F. Jaramillo, K.P. Jørgensen, J. Bonde, J.H. Nielsen, S. Hørch, Ib. Chorkendorff, Identification of active edge sites for electrochemical H<sub>2</sub> evolution from MoS<sub>2</sub> nanocatalysts, *Science* 317 (2007) 100–102.
- [62] R. Addou, S. McDonnell, D. Barrera, Z. Guo, A. Azcat, J. Wang, H. Zhu, C.L. Hinkle, M. Quevedo-Lopez, H.N. Alshareef, L. Colombo, J.W.P. Hsu, R.M. Wallace, Impurities and electronic property variations of natural MoS<sub>2</sub> crystal surfaces, *ACS Nano* 9 (2015) 9124–9133.
- [63] Y. Li, H. Wang, L. Xie, Y. Liang, G. Hong, H. Dai, MoS<sub>2</sub> nanoparticles grown on graphene: an advanced catalyst for the hydrogen evolution reaction, *J. Am. Chem. Soc.* 133 (2011) 7296–7299.
- [64] A. Jiang, B. Zhang, Z. Li, G. Jin, J. Hao, Vanadium doped WS<sub>2</sub> nanosheets grown on carbon cloth as highly efficient electrocatalyst for hydrogen evolution reaction, *Chem. Asian J.* 13 (2018) 1438–1446.
- [65] A.W. Bott, Electrochemistry of semiconductors, *Curr. Sep.* 17 (1998) 87–92.
- [66] A.J. Bard, L.R. Faulkner, *Electrochemical Methods: Fundamentals and Applications*, John Wiley and Sons Inc., New York, 2000.
- [67] K. Gelderman, L. Lee, S.W. Donne, Flat-band potential of a semiconductor: using the mott–schottky equation, *J. Chem. Educ.* 84 (2007) 685.
- [68] A.A. Tedstone, D.J. Lewis, P. O'Brien, Synthesis, properties, and applications of transition metal-doped layered transition metal dichalcogenides, *Chem. Mater.* 28 (2016) 1965–1974.
- [69] R. Heyrovská, Atomic, ionic and Bohr Radii linked via the golden ratio for elements of groups 1–8 including lanthanides and actinides, *Int. J. Sci.* 2 (2013) 63–68.
- [70] M. Sharon, A. Sinha, Effect of electrolytes on flat band-band potential of n-BaTiO<sub>3</sub> semiconductor, *Electrochim. Acta* 28 (1983) 1063–1066.
- [71] R. Beranek, (Photo) electrochemical methods for the determination of the band edge positions of TiO<sub>2</sub>-Based nanomaterials, *Adv. Phys. Chem.* (2011) 1–20.
- [72] F.S.B. Kafi, K.M.D.C. Jayathileka, R.P. Wijesundera, W. Siripala, Fermi-level pinning and effect of deposition bath pH on the flat-band potential of electrodeposited n-Cu<sub>2</sub>O in an aqueous electrolyte, *Phys. Status Solidi B* 253 (2016) 1965–1969.